Supplementary Information for: Multidimensional Nano-Imaging of Structure, Coupling, and Disorder in Molecular Materials

Sven A. Dönges,[1,2] R. Peyton Cline,[2] Steven E. Zeltmann,[3] Jun Nishida,[1,2] Bernd Metzger,[1,2] Andrew M. Minor,[3,4] Joel D. Eaves,[2] and Markus B. Raschke[1,2]

[1]*Department of Physics and JILA, University of Colorado, Boulder, CO 80309*

[2]*Department of Chemistry, University of Colorado, Boulder, CO 80309*

[3]*Department of Materials Science and Engineering, University of California, Berkeley, CA 94720, USA*

[4]*National Center for Electron Microscopy, Molecular Foundry, Lawrence Berkeley, National Laboratory, Berkeley, CA 94720, USA*

I. METHODS

IR *s*-SNOM a Yb:KGW oscillator (FLINT, Light Conversion) with a repetition rate of 76MHz is used to pump a perodically-poled lithium niobate (PPLN) optical paramteric oscillator (OPO) (Levante, APE GmbH). Through difference frequency generation between the signal and idler outputs of the OPO in a $AgGaS_2$ crystal (HarmoniXX, APE GmbH), tunable broadband mid-infrared (mid-IR) pulses with a bandwidth of $\approx 150\,\mathrm{cm}^{-1}$ are generated. To cover both the symmetric and antisymmetric stretch modes of PTFE the mid-IR laser output is tuned to $\approx 1200\,\mathrm{cm}^{-1}$. To avoid tip or sample damage in the IR *s*-SNOM measurements the infrared radiation is attenuated to $60 - 80\,\mathrm{pJ}$ pulse energies using wire grid mesh filters.

Using conventional reflective optics, the mid-IR light is directed into a *s*-SNOM instrument (nanoIR2-s prototype, Anasys Instruments/Bruker) [1] modified with a custom built Peltier based sample heating/cooling stage to allow for continuous sample temperature adjustments between 10 °C and 40 °C. Using a 90 ° off-axis parabolic mirror ($f = 25.4\,\mathrm{mm}$, NA = 0.45), the mid-IR light is focused onto the apex of a gold coated silicon AFM tip (160AC-GG, MikroMasch). By adjusting the light polarization parallel to the axis of the tip, optimum coupling of the light to the tip is ensured. The light scattered from the tip is collected with the same off axis parabolic mirror and directed onto HgCdTe detector (KLD-0.5-J1/11, Kolmar Technologies) where it is heterodyne amplified with an unmodified reference field. The detected signal is demodulated at the second harmonic of the AFM tip tapping frequency using a lock-in amplifier (HF2LI, Zurich instruments) to discriminate between near-field and far-field contributions to the signal [2].

By changing the time delay between scattered and reference signal using a translation stage (ANT95-50-L-MP, Aerotech) moved at speeds of $0.01 - 0.03\,\mathrm{mm/s}$ an interferogram of the tip scattered light is collected at acquisitions times of $5 - 17\,\mathrm{ms}$ per data point. Complex valued spectra were calculated from the interferograms by performing Fourier transforms. By fitting the sum of two complex valued Lorentzians to the real $\mathcal{F}'_{\mathrm{N}}$ and imaginary $\mathcal{F}''_{\mathrm{N}}$ part of the spectra, seven independent fitting parameters were calculated for each spectrum (amplitudes a_{S},a_{AS}; linewidth Γ_{S},Γ_{AS}; and center frequency $\bar{\nu}_{\mathrm{S}}$, $\bar{\nu}_{\mathrm{AS}}$ for the symmetric (S) and antisymmetric (AS) stretch modes, and a background term ϵ_∞). Complex valued Lorentzian fits gave consitently the best and most robust fit results. However, selected spectra were

also fit to established tip-sample interaction models (point [3] and finite [4, 5] dipole models) to rule out that any observed spectral trends are caused by artifacts of the tip sample interaction. During these tests, no evidence of systematic spectral variations due to the tip sample interaction could be identified (see supplement section IV A). For hyperspectral mapping of the sample, interferograms were collected in two-dimensional grids with grid sizes ranging from 20×20 to 50×50 interferograms and grid spacing of $50 - 100\,\mathrm{nm}$.

4D-STEM Four-dimensional scanning transmission electron microscopy [6] (4D-STEM) was acquired using an FEI TitanX operated at 300 kV and using a probe semi-convergence angle of $24\,\mu\mathrm{rad}$. All TEM data collection was conducted with the sample cooled to approximately $-180\,^{\circ}\mathrm{C}$ using a liquid nitrogen sample holder to reduce damage caused by the electron beam. A 100×100 pixel grid was scanned with 20 nm steps, and a 512×512 pixel electron diffraction pattern was recorded at each scan point. Local peaks in the diffraction patterns arising from Bragg diffraction of Teflon crystallites were identified using cross-correlation with a template image. Detected Bragg reflections inside the first diffraction ring are used to determine the local chain orientations using the flowline method of [7]. The flowlines are "seeded" at locations of high diffraction intensity and propagate in the direction of the local chain alignment in order to visualize the interpenetrating domains of different chain orientation. Pixelwise cross-correlations are used to determine the correlation lengths for similar orientations and different misorientations [7].

DFT We use the Vienna Ab initio Simulation Package (VASP) to compute the DFT results [8–13]. Our calculations employ the projector augmented wave method and the exchange-correlation functional with the Perdew-Burke-Ernzerhof (PBE) generalized gradient approximation [10, 13]. We use the standard C and F pseudopotentials supplied by VASP, which treat explicitly the $(2s)^2(2p)^4$ electrons for both potentials. For sampling the Brillouin zone, we use four k-points along the reciprocal lattice vector conjugate to the length of the PTFE strands and one k-point in the other two directions.

We set the plane-wave cutoff to 1040 eV, or 2.6 times the default cutoff. We use this large basis set because it converges the energy to less than 1 meV/atom, which we demand to ensure accurate calculations. We require an electronic convergence of 10^{-7} eV and a minimum of 10 electronic steps when minimizing the electronic structure. Because we calculate the phonon spectrum for our strands of PTFE, we set the precision-mode to accurate and adjusted the fine FFT grids to reduce the noise in the forces. We require a

final force convergence of 5×10^{-5} eV/Å for the atomic positions of both the 13_6 and 15_7 helical conformations.

Before relaxing the atomic positions to the desired force convergence, we first relaxed the length of the PTFE strands by allowing the unit cell lattice constant in that direction to change. We modified and employed the function `constr_cell_relax.F` supplied with VASP to restrict a full geometry relaxation (atomic positions, cell shape, cell volume) to change *only* the atomic positions and the desired lattice constant. We required a force convergence of 10^{-4} eV/Å for the 13_6 helix and 10^{-3} eV/Å for the 15_7 helix for this "restricted-full" relaxation.

We use the nonlinear least-squares algorithm `lsqnonlin` in MATLAB to fit each DFT-calculated spectrum to the model Hamiltonian spectrum. We ensure that the minimizer arrived at the output state: "Optimization completed because the size of the gradient is less than the value of the optimality tolerance" which we set to the default value. We also employed "central" finite differences, which is more accurate than the default "forward" setting.

II. TRANSITION DIPOLE MOMENT ESTIMATE

We estimate the transition dipole moment (TDM) of PTFE by determining the TDM of an individual CF unit using the fluorinated polymer 1H,1H,2H,2H-Perfluorodecanethiol ($CF_3(CF_2)_7CH_2CH_2SH$) which is soluble in carbontetracloride (CCl_4) and contains seven CF_2 and one CF_3 functional groups. We perform transmission Fourier transform infrared (FTIR) spectroscopy of three solutions of $n_1 = 52\,\text{mmol/l}$, $n_2 = 111\,\text{mmol/l}$, and $n_3 = 231\,\text{mmol/l}$ of 1H,1H,2H,2H-Perfluorodecanethiol in CCl_4 using a cell of $6\,\mu$m thickness.

Fig. S1 shows the collected FTIR absorbance spectra referenced against an FTIR spectrum of pure CCl_4. In good agreement with literature, we assign the spectral features at $\approx 1150\,\text{cm}^{-1}$, $\approx 1215\,\text{cm}^{-1}$, and $\approx 1240\,\text{cm}^{-1}$ to the symmetric stretch of CF_2, the antisymmetric stretch of CF_2, and the antisymmetric stretch of CF_3, respectively [14, 15].

We then use the spectral integral of the spectra to estimate the TDM of a single CF_2

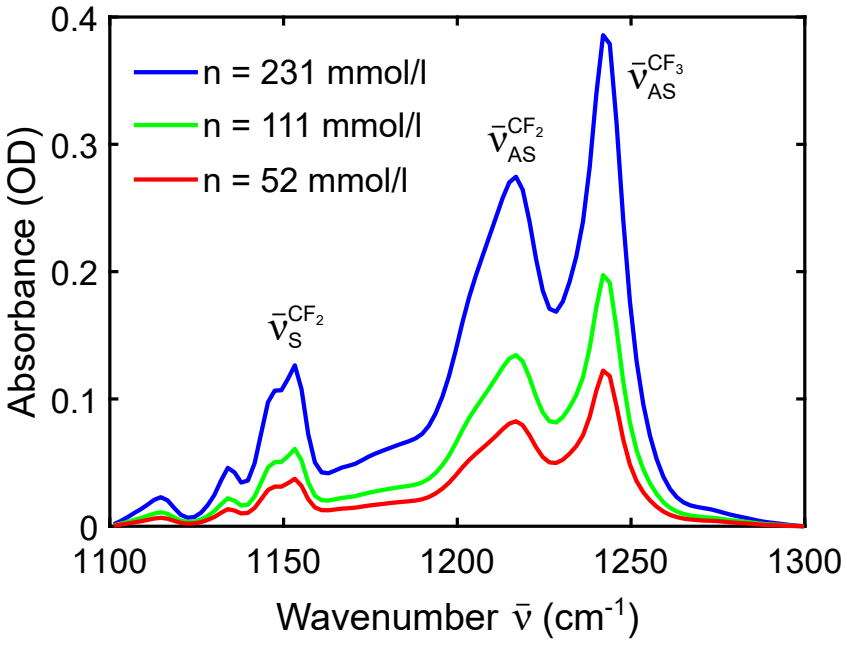

Figure S1: FTIR absorbance spectra for three different concentrations of 1H,1H,2H,2H-Perfluorodecanethiol.

based on equations for the dipole moment of a transition from [16]:

$$\mu_{21}^2 = 3\,\frac{g_1}{g_2}\,\frac{\epsilon_0 \hbar c}{\pi \omega_{21}}\,\sigma_0 \tag{1}$$

where μ_{21} is the transition dipole moment (TDM), g_1 and g_2 the degeneracy factors of the ground and excited state, ϵ_0 the vacuum permittivity, $\hbar$ reduced Planck constant, c the speed of light, and ω_{21} the vibrational frequency. The absorption cross-section σ_0 is given in terms of the absorbance spectrum $A(\omega)$ by:

$$\sigma_0 = \int_{-\infty}^{\infty} \frac{A(\omega)}{\log_{10}(e^1)\,L\,n}\,d\omega \tag{2}$$

where L is the sample thickness, and n number concentration of molecules.

With $g_1 = g_2 = 2$, $\omega_{21} = 1200\,\mathrm{cm}^{-1}$ as the approximate average frequency, and $L = 6\,\mu\mathrm{m}$, we obtain $\mu_{avg} = 1.06\,\mathrm{D}$. As in linear spectroscopy the total TDM of a coupled ensemble of oscillators is conserved from the individual modes we can estimate the TDM of an individual CF oscillator as $\mu_{\mathrm{CF}} = 0.26\,\mathrm{D}$.

From the crystal structure of PTFE in the 15_7 conformation we can calculate the TDM per unit volume of PTFE. PTFE forms an orthorhombic lattice with hexagonal symmetry in the a-b plane with lattice constant 0.57 nm. In the c-direction the structure repeats after 1.97 nm

every 15 CF_2 units. Therefore there are 30 CF units in a volume of $1.97 \times 0.57 \times 0.49\,\mathrm{nm}^3 = 0.55\,\mathrm{nm}^3$. The TDM density is then $\sqrt{30} \times 0.26\,\mathrm{D}/0.55\,\mathrm{nm}^3 = 2.6\,\mathrm{D/nm}^3$ for PTFE. This value is significantly higher than the corresponding value of approximately $1\,\mathrm{D/nm}^3$ for, e.g. an already strong carbonyl vibration in a ruthenium carbonyl complex [17].

From our DFT calculations we know that the relative strength of the TDMs of the delocalized symmetric and antisymmetric stretch modes of PTFE are $\mu_\mathrm{S}/\mu_\mathrm{AS} = 0.57$. Since the delocalized modes are each doubly degenerate, $\mu_\mathrm{S} = 0.91\,\mathrm{D/nm}^3$ and $\mu_\mathrm{AS} = 1.60\,\mathrm{D/nm}^3$.

For comparison we can also calculate $\mu_\mathrm{S}^\mathrm{theo}$ and $\mu_\mathrm{AS}^\mathrm{theo}$ from the dipole-dipole coupling constant $\lambda = \frac{(\mu_\mathrm{CF}^\mathrm{theo})^2}{8\pi^2\hbar c\epsilon_0\epsilon x_0^3} = 90\,\mathrm{cm}^{-1}$ in our vibrational exciton model, with $x_0 = 1$ Å (as used in the modelling calculations) and $\epsilon \approx 1.5$ [18]. Thus we calculate $\mu_\mathrm{CF}^\mathrm{theo} = 0.16$ and consequently $\mu_\mathrm{S}^\mathrm{theo} = 0.57\,\mathrm{D/nm}^3$ and $\mu_\mathrm{AS}^\mathrm{theo} = 1.0\,\mathrm{D/nm}^3$. In fairly good quantitative agreement with the experimentally determined TDM our vibrational exciton model predicts a TDM only $\approx 40\%$ smaller than the experimentally determined value.

III. EXTENDED HYPERSPECTRAL HETEROGENEITY

In addition to the datasets presented in Figs. 2 and 4 in the main text, we collected hyperspectral data on different locations on the same aggregate of melted PTFE, as well as multiple other PTFE aggregates. Fig. S2 shows hyperspectral data collected in a different location of the same melted PTFE aggregate as in Fig. 2 of the main text. The general topographic structure (Fig. S2A) is very similar, with long strands of PTFE with bare substrate areas in between and smaller islands of PTFE of varying sizes. Fig. S2B shows the spatial variation of the antisymmetric stretch frequency ν_{AS} in the region indicated by the dashed square in panel A. Similar to the data presented in Figs. 2 and 4 of the main text, ν_{AS} varies over more than $30\,\mathrm{cm}^{-1}$ on lengths scales of a few hundred nm. A subset of data (red points in Fig. S2B) are selected by identifying spectra that show within the laser bandwidth a minimum in the imaginary part of the spectrum blue of ν_{AS}. This method predominantly identifies spectra taken in areas with smaller islands of PTFE. Fig. S2C shows the correlation plot between the symmetric stretch frequency ν_S and ν_{AS} as shown in B. Similar to the data presented in the main text, a strong correlation between the two frequencies is observed and a small subset of spectra at the bottom and bottom right of the hyperspectral image show higher vibrational frequencies for low topography areas. However,

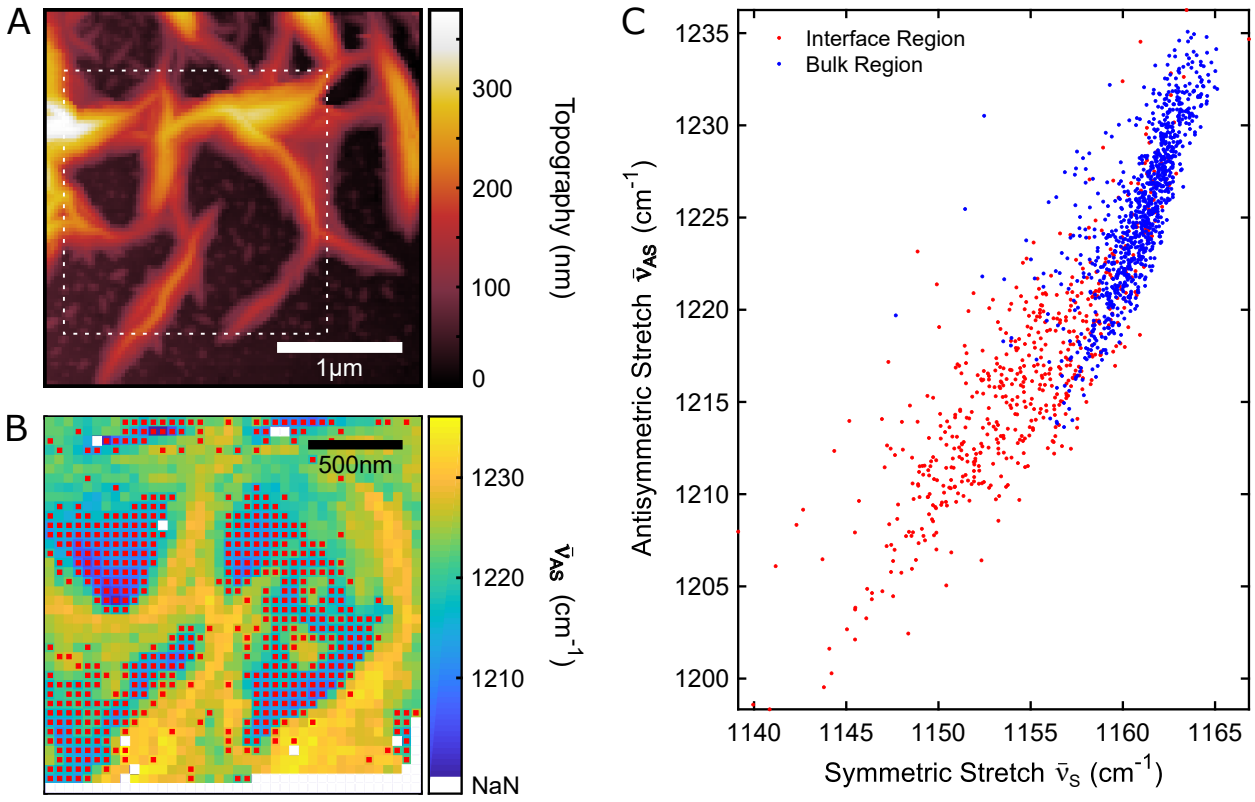

Figure S2: **A**. AFM topography at the edge of a PTFE bead. **B** nano-FTIR image of the spatial variation in the antisymmetric stretch mode peak position ($\bar{\nu}_{\mathrm{AS}}$) indicated by the white dashed square in A. **C**. Correlation plot between $\bar{\nu}_{\mathrm{S}}$ and $\bar{\nu}_{\mathrm{AS}}$. The subset of red datapoints is indicated by red squares in A and selected by identifying spectra with a spectral minimum blue of ν_{AS}.

in contrast to the data presented in the main text, the majority of datapoints associated with small PTFE islands or PTFE at the interface between high topography areas and the gold substrate (red) exhibit lower vibrational frequencies than spectra recorded in locations with high topography (blue).

This kind of spectral behavior cannot be explained with the nano-scale models of PTFE presented in the main text and highlights the high level of nanoscale complexity even in a comparably simple polymer like PTFE.

In addition, Fig. S3 shows the ν_S-ν_{AS} correlation density plots for all dataset collected on the melted PTFE samples together with datasets collected on the microtomed samples. The majority of these datasets were collected at or close to the center of an island of melted PTFE. Different colors indicate specific circumstances like datasets collected below (blue) or above (red) room temperature, or on microtomed samples. for each dataset we continue

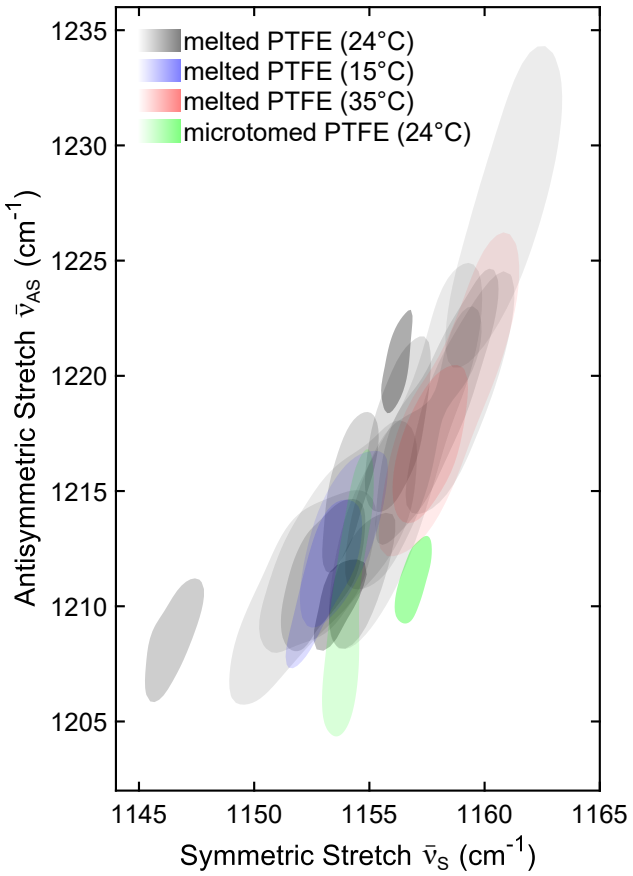

Figure S3: Density correlation plot between $\bar{\nu}_{\mathrm{S}}$ and $\bar{\nu}_{\mathrm{AS}}$ for each collected dataset.

to observe a strong correlation between ν_S and ν_{AS} as well as a strong correlation between the two frequencies when combining the spectra from all datasets.

IV. NANOMECHANICAL PROPERTY MAPPING

In addition to conventional dynamic mode AFM, we also performed peak force nanomechanical mapping (MultiMode 8, Bruker) to measure spatial variations in the adhesion, deformation, and dissipation of the tip sample interaction [19, 20]. In general, this method also allows for quantitative extraction of the sample properties through calibration of the tip [21], however, on our PTFE sample, the tip apex became unstable within few minutes of scanning so that calibrated measurements could not be performed. Nonetheless, even the uncalibrated measurements show very specific contrast.

Fig. S4 shows peak force nanomechanical mapping for approximately the same sample location as shown in Fig. 2 of the main text. Fig. S4A shows the sample topography where

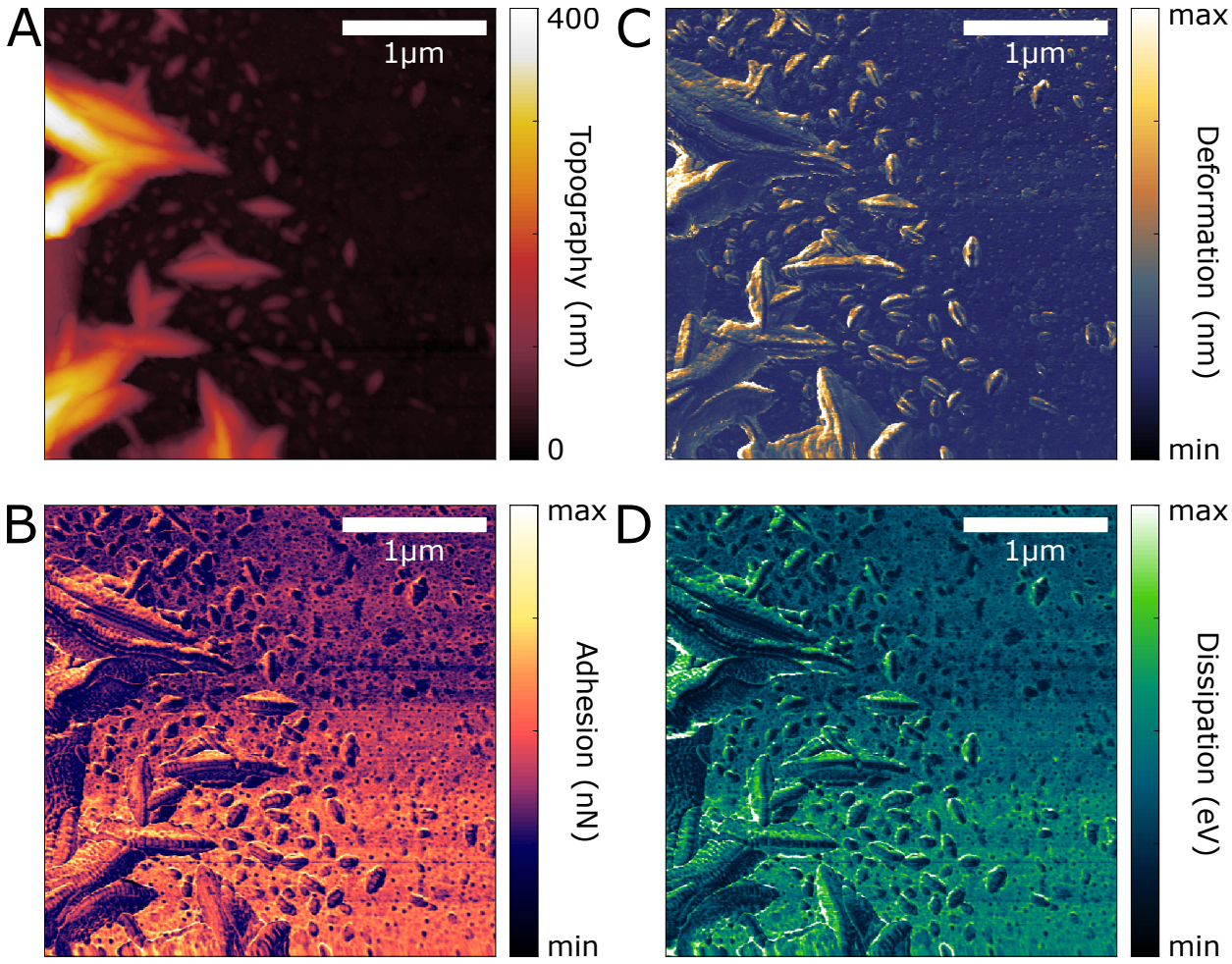

Figure S4: Sample **A**. Topography, **B**. Adhesion, **C**. Deformation, and **D**. Dissipation in approximately the same sample location as shown in Fig. 2 of the main text.

low areas (dark) correspond to the gold substrate and higher areas (bright) correspond to PTFE nano- and micro-islands and -strands with varying thickness. In addition to topography, the deformation, adhesion, and dissipation of the tip sample interaction (Fig. S4B-D) show contrast within individual islands of PTFE. Specifically, in most PTFE nano-islands the deformation, adhesion and dissipation are anisotropic. This is not an artifact of the scan direction as the same contrast can be reproduced when rotating the scan direction by 90° (data not shown). In addition, larger PTFE strands (left side of image) show a weakly striped contrast perpendicular to the primary strand direction. With sizes of 20-30 nm these features on the larger PTFE strands are at the resolution limit of our nano-spectroscopy measurements which is given approximately by the tip apex radius of our metallized AFM tips. With $50 - 100$ nm point spacing for our nano-spectroscopic data arrays we are not

resolving these features.

These nanomechanical maps of our PTFE samples further underline the structural and morphological heterogeneity we discovered in our hyperspectral measurements. The spectral the differences are observed to primarily correlate with the PTFE island, caused by the variations in island sizes. In contrast, the nanomechanical properties vary equally across islands of different sizes with multiscale heterogeneities present from ten to hundreds of nm feature size, many at or below the resolution of our nano-FTIR measurements. This suggests additional complexity in this simple polymer beyond those identified in the main text and highlights the importance of multimodal and multiscale measurements.

V. NEAR-FIELD INTERACTION BETWEEN TIP AND SAMPLE

A. Tip Sample Interaction with Negligible Impact on Nano-FTIR Characteristics

The near-field interaction between tip and sample is known to cause the red-shift of a near-field spectrum compared to the corresponding far-field spectrum [4, 5]. We have evaluated the influence of this effect in our data by fitting the real and imaginary component of several

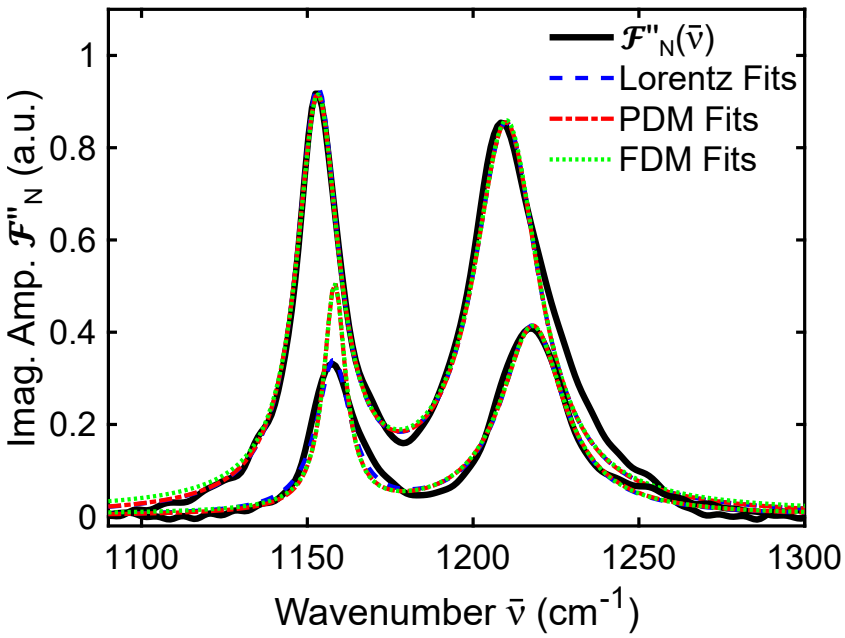

Figure S5: Lorentzian fits (blue dashed), point dipole model (PDM, red dot-dashed), and finite dipole model (FDM, green dotted) all fit the experimental data well.

selected near-field spectra with different models. The functional form underlying all our fits is the sum of two complex valued Lorentzian resonances and a non-resonant dielectric background term ϵ_∞, representing the observed two molecular resonances in the investigated spectral region ($1100 - 1300\,\mathrm{cm}^{-1}$). Thus, there are seven independent fit parameters for each spectrum (as described in the main text). We find that fits with the point [3] and finite [4] dipole near-field interaction models fit the data equally well. Not taking into account a tip interaction model (far-field like fits), by fitting the pure functional form to the data generates good fits, too. Both tip interaction models show systematically $1 - 3\,\mathrm{cm}^{-1}$ higher frequencies for both resonances, compared to the far-field like fits. While the actual frequencies differ slightly between the fitting procedures the overall frequency spread across individual datasets remains unchanged because the frequency shift for fitting with different models is consistent across the entire dataset. The resonance linewidths and amplitude ratios between the peaks remain largely the same between different fitting procedures. We thus conclude that the influence of the AFM tip on the near-field spectra is negligible and does not effect the observed spectral trends.

B. Plasmonic Field Enhancement in the Tip-Sample Junction

As discussed before, the thickness of PTFE on our samples varies continuously from several hundred nm in some areas to no PTFE in other areas. It is well established that the gold substrate plasmonically enhances the near-field signal for thin layers of probe material [22]. To rule out that the spectral variations we observe in PTFE are caused by enhanced electric fields between the tip and sample altering the vibrational modes we acquired near-field spectra at different laser pulse energies. The results for two different locations are shown in Fig. S6 for laser pulse energies varying by approximately one order of magnitude. All spectra are normalized to the amplitude of the antisymmetric stretch frequency for easier comparison. The dotted spectra in Fig. S6 are acquired on top of a thick strand of PTFE at least 200 nm thick. This thickness ensures that no field enhancement from the gold substrate is affecting the spectra. The dashed spectra were recorded in an area with very small islands of PTFE with topographic heights of less than 10 nm. Neither set of spectra show a systematic variation of the symmetric and antisymmetric stretch frequencies with the pulse energy of the laser. Any variation in $\bar{\nu}_\mathrm{S}$ and $\bar{\nu}_\mathrm{AS}$ present in these spectra we attribute

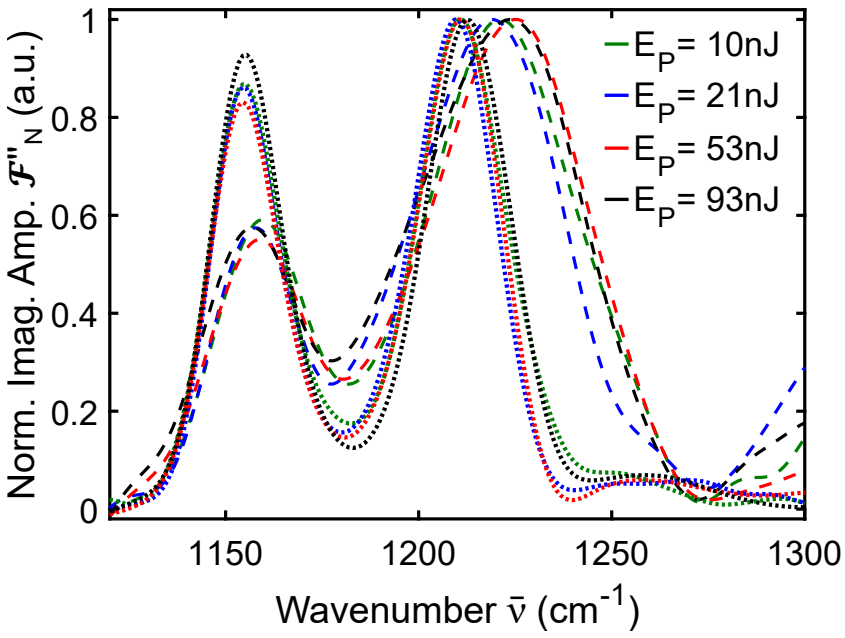

Figure S6: Power dependent near-field spectra on top of bulk (dotted) and interfacial (dashed) PTFE.

to sample drift while the spectra were recorded, especially as the variations in the spectra do not correlate with the change in incident laser pulse energies. As our experiments are performed with pulse energies between $50 - 60\,\mathrm{nJ}$ we conclude that the local electric field and local electric field enhancement do not play a role in causing the spectral variations we observe.

VI. X-RAY DIFFRACTION

While four dimensional scanning transmission electron microscopy (4D-STEM) is capable of measuring the crystal orientation in a thin sample of PTFE in three dimensions and with tens of nm resolution, it is insensitive to the actual crystal lattice spacing. To confirm the polycrystalline structure of melted PTFE grazing incidence micro-XRD (GI-μXRD) data were collected using a Rigaku D/Max Rapid II instrument equipped with a two-dimensional image plate detector. X-rays were generated by a MicroMax 007HF generator fitted with a rotating chromium anode ($\lambda = 2.2897$ Å) that was focused on the specimen through a $300\,\mu$m-diameter collimator. The correct sample-to-detector distance was verified by measuring the lattice constant of a LaB6 standard (NIST 660c). To ensure data reproducibility,

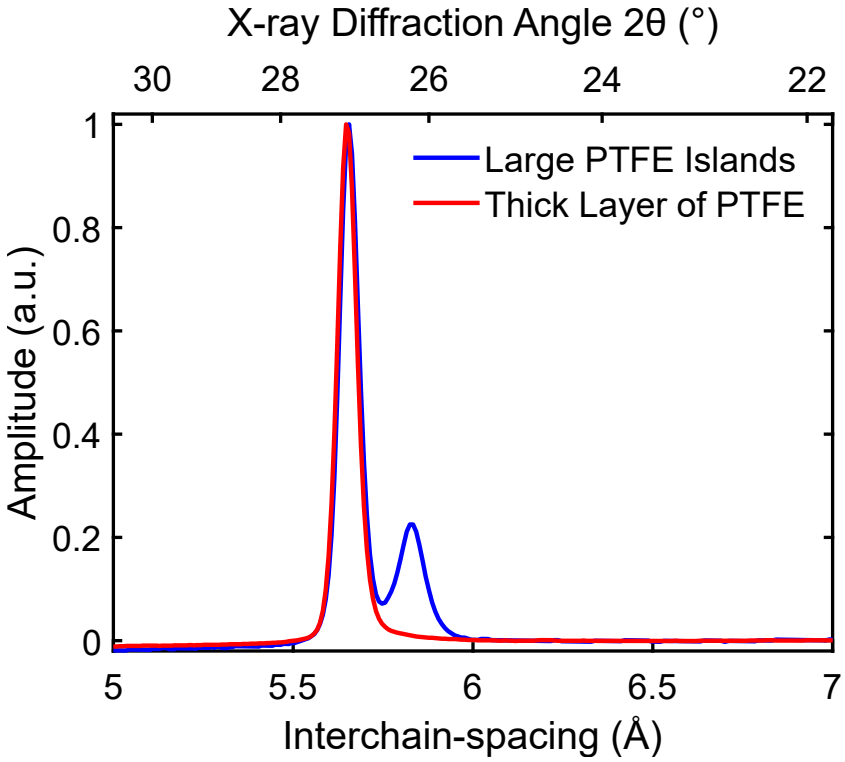

Figure S7: XRD diffraction spectrum for melted PTFE.

the experiments were repeated at multiple spots that yielded similar results. XRD patterns were collected at a fixed 1 degree incident angle with no sample rotation in the sample plane. Rigaku's 2D Data Processing Software (v.1.0, Rigaku, 2007) was used to integrate the diffraction rings captured by the detector.

Fig. S7 shows XRD measurements on a melted PTFE layer estimated to be tens of μm thick (red), as well as an XRD measurement on a smaller island of melted PTFE (blue). While the blue XRD spectrum was taken on an island similar to the one shown in Fig. 2 of the main text, the island investigated in the XRD measurements is significantly larger than the one we performed *s*-SNOM on and at the center estimated to be more than 1 μm thick. This choice of island for the XRD measurements was necessary because of the large focus size of the X-ray beam as on smaller islands the signal level was too low. While on the top the measured X-ray diffraction angle 2θ is displayed, the bottom x-axis shows the calculated interchain spacing in PTFE, assuming a perfectly hexagonal cross section of the PTFE crystal.

The XRD spectrum on the thick sample shows a single dominant peak for an interchain spacing of 5.65 Å in good agreement with literature values for the interchain spacing in

form IV [23, 24]. This same peak is also present in measurements on the island of PTFE, however, an additional, yet weaker, peak at an interchain spacing of 5.82 Å is also present. This additional peak cannot be associated with the template stripped gold layer, the silicon substrate, or a potential native oxide layer on the silicon substrate. Therefore, we conclude that it is related to PTFE, although, to our knowledge, no PTFE structure with a lattice spacing of 5.82 Å has been reported in literature. Compared to some other samples we prepared the displayed spectra show a high level of crystallinity, as hardly any background signal could be detected. Some of our other samples (spectra not shown here) that we did not perform *s*-SNOM measurements on showed none or much weaker peaks at the interchain spacing of PTFE, but often showed a very broad background around an interchain spacing of 5.5 Å that we associate with a largely amorphous PTFE sample.

Using the Scherrer equation

$$\tau = \frac{K\,\lambda}{\beta\,\cos\theta} \tag{3}$$

the XRD spectra can be used to estimate the crystallite size in our PTFE samples. Here τ is the size of the crystallites, K a dimesnionless shape factor estimated to be $K = 0.9$, λ the XRD wavelength, β the full width of half maximum (in radians) of the observed XRD peak, and θ the Bragg angle. With $\lambda = 2.2897$ Å, $\beta = 0.33\,^\circ$, and $\theta = 27.08\,^\circ$ we estimate the PTFE crystallites to be on the order of 40 nm.

VII. VIBRATIONAL DELOCALIZATION

The large frequency variations observed in the experiments as well as the strong interactions calculated through simulation and modelling raise the question to what extent the delocalization of the coupled modes along the chain affects the spectral characteristics. We thus calculate the impact of dipole-dipole coupling between the individual CF_2 groups in the PTFE chain (based on their actual position and orientations with respect to each other) on the vibrational modes and frequencies of different numbers of coupled CF_2 groups.

For numbers of coupled CF_2 groups Fig. S8 shows all calculated vibrational frequencies for both the symmetric (red) and antisymmetric (blue) stretch modes. However, most are not infrared active and can thus not be detected in our experiments. Fig. S8 shows that a distribution of different chain lengths in the sample results in an anti-correlation between $\bar{\nu}_{\mathrm{S}}$ and $\bar{\nu}_{\mathrm{AS}}$ for very small chain lengths, and a flat correlation for larger chain lengths.

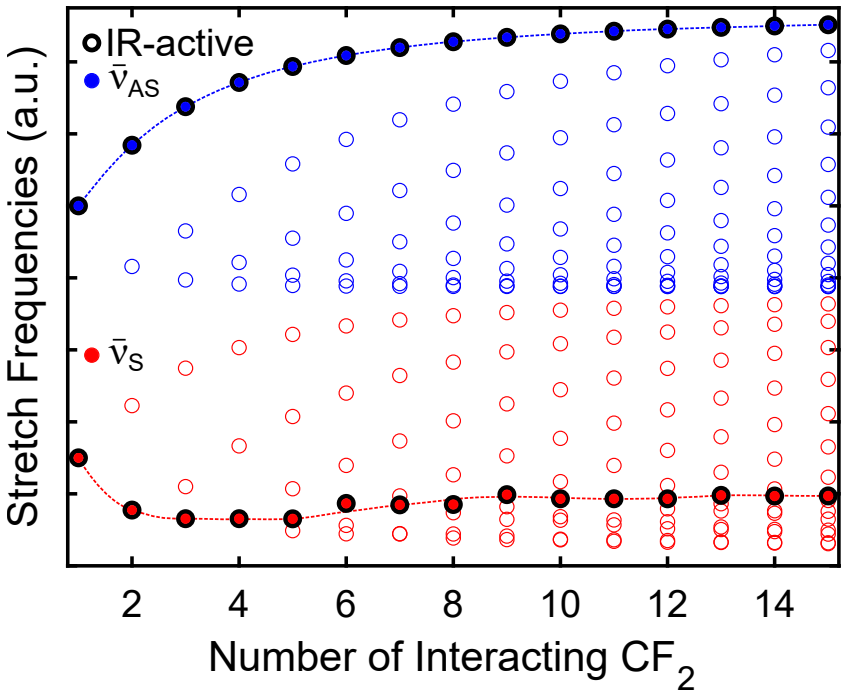

Figure S8: Evolution of $\bar{\nu}_{\mathrm{S}}$ and $\bar{\nu}_{\mathrm{AS}}$ for different number of interacting CF_2 functional groups.

Thus, compositional heterogeneity, caused by phase segregation of PTFE with different chain lengths, is an improbable cause for the observed strong spectral correlation between $\bar{\nu}_{\mathrm{S}}$ and $\bar{\nu}_{\mathrm{AS}}$ (Fig. 2 of the main text), as compositional heterogeneity would lead to anti-correlated spectral peak shifts.

VIII. VIBRATIONAL EXCITON MODEL

Here we provide additional details of the vibrational exciton model developed in the main text. As described in the main text the Hamiltonian for our vibrational exciton model becomes:

$$\mathcal{H} = \nu \sum_{l} a_l^\dagger a_l + \frac{J}{2} \sum_{\langle l,l' \rangle} (a_l^\dagger a_{l'} + a_{l'}^\dagger a_l) + \frac{\lambda}{2} \sum_{k,l \neq k} V_{kl} \left(a_k^\dagger a_l + a_l^\dagger a_k \right). \tag{4}$$

The first term is the sum over the local mode vibrational frequencies, with each C–F oscillator taken to have the same energy. The second term is the through-bond coupling, with the notation $\sum_{\langle l,l' \rangle}$ referring to the sum over pairs of local modes attached to the same carbon. The third term is the through-space coupling, parameterized by $\lambda = \frac{\mu^2}{4\pi\epsilon_0 \epsilon x_0^3}$ and mediated through the transition dipole-transition dipole tensor, $V_{kl} = \hat{\boldsymbol{m}}_k \cdot \left(\frac{\mathbf{1} - 3\hat{r}_{kl}\hat{r}_{kl}}{r_{kl}^3} \right) \cdot \hat{\boldsymbol{m}}_l$, where $\boldsymbol{r}_{kl}$ is the vector between the centers of the point transition dipoles $\boldsymbol{m}_k$ and $\boldsymbol{m}_l$ that are centered

at $\boldsymbol{r}_k$ and $\boldsymbol{r}_l$, respectively. Hats denote unit vectors and $V_{kl} = 0$ for oscillators attached to the same carbon. Note that the expression for the the dipole-dipole coupling between *transition dipoles*, V_{kl}, is the same as the dipole-dipole coupling between *static dipoles*.

The *normal modes* of oscillation have creation and annihilation operators, $\{b_\alpha, b_\alpha^\dagger, \cdots\}$ that are linear combinations of those for the local modes, $b_\alpha = \sum_l U_{l,\alpha} a_l$, that diagonalize the Hamiltonian, $\mathcal{H} = \sum_\alpha \epsilon_\alpha b_\alpha^\dagger b_\alpha$. The total, far-field spectrum comes from the Golden rule, $I(\omega) \propto \sum_\alpha \langle 0|\boldsymbol{m}|\alpha\rangle\langle\alpha|\boldsymbol{m}|0\rangle\delta(\hbar\omega - \epsilon_\alpha)$, where $\boldsymbol{m}$ is the total dipole moment of the system. The parameters ν, J, and λ can be determined by fitting the far-field spectrum of the exciton model to the vibrational absorption spectrum computed from DFT. The three-parameter model exciton Hamiltonian provides an excellent fit to those data.

Performing a fit of the model Hamiltonian $\mathcal{H}$ to the vibrational mode structure caluclated by DFT yields model parameters $\nu = 1143.7\,\mathrm{cm}^{-1}$ and $\nu = 1146.5\,\mathrm{cm}^{-1}$ for the 13_6 and 15_7 helical configurations respectively. The coupling parameters are fit to be $J = -7.3\,\mathrm{cm}^{-1}$ and $\lambda = 89.3\,\mathrm{cm}^{-1}\text{Å}^3$.

From this we can move towards an idealized version of the experiment. The *s*-SNOM experiment probes the optical polarization as a function of position. The polarization around point $\boldsymbol{r}$ in the frequency domain is $\boldsymbol{P}(\boldsymbol{r},\omega) = \boldsymbol{\chi}(\boldsymbol{r},\omega) : \boldsymbol{E}(\omega)$, where the susceptibility at point $\boldsymbol{r}$ and frequency ω, $\boldsymbol{\chi}(\boldsymbol{r},\omega)$, comes from the dipole moments surrounding point $\boldsymbol{r}$. The susceptibility is the Fourier-Laplace transform of the linear response function, $-\frac{i}{\hbar}\langle[\boldsymbol{\mu}_{\boldsymbol{r}}(t), \boldsymbol{\mu}_{\boldsymbol{r}}(0)]\rangle$. Simple algebra shows that the response function depends on the quantum correlation functions $\langle a_l^\dagger(t) a_k(0)\rangle$, where l and k correspond to local mode oscillators in the neighborhood of point $\boldsymbol{r}$. Interestingly, while the operators are spatially local, their time evolution depends on the eigenstates of $\mathcal{H}$—the normal modes—which are generally nonlocal. It is a straightforward calculation to go from the spatially-resolved quantum time-correlation function to the spatially-resolved optical absorption spectrum [25].

We then compute an idealized experiment probing a single PTFE strand within a crystal of aligned PTFE molecules. We construct a hexagonal lattice of finite size to represent microcrystaline PTFE, with PTFE molecules parallel to each other with a uniform interchain distance of 5.7 Å. Importantly, the lattice is nonperiodic in the directions *perpendicular to* the strands. To minimize computational complexities, we neglect slight deviations from the perfectly hexagonal structure in both form II and form IV [24, 26, 27]. When computing the spatially-resolved optical spectrum, we calculate the spectrum from a single strand at

a time, and find that vibrational frequencies of an isolated PTFE chain are blue-shifted by $\Delta\bar{\nu}_{\mathrm{S}} \approx 6\,\mathrm{cm}^{-1}$ and $\Delta\bar{\nu}_{\mathrm{AS}} \approx 13\,\mathrm{cm}^{-1}$ compared to lattice bound molecules in the interior (Fig. 5 of the main text).

To interpret these results, note that for a strand located at point $\boldsymbol{r}$ with transition dipole moment $\boldsymbol{m}_{\boldsymbol{r}}$, the Hamiltonian can be written in a form that emphasizes the connection to classical linear response theory for solvation. $\mathcal{H} = H_0 + \boldsymbol{m}_{\boldsymbol{r}} \cdot \boldsymbol{P}(\boldsymbol{r})$, where H_0 is the local Hamiltonian for all oscillators within the strand at $\boldsymbol{r}$ and $\boldsymbol{P}(\boldsymbol{r}) = \frac{1}{2}\sum_{\boldsymbol{r}'\neq\boldsymbol{r},\boldsymbol{r}'} \boldsymbol{T}_{\boldsymbol{r},\boldsymbol{r}'} : \boldsymbol{m}_{\boldsymbol{r}'}$, where $\boldsymbol{T}$ is the dipole-dipole tensor, is the polarization field from all molecules outside point $\boldsymbol{r}$. In this form, the Hamiltonian is precisely that of a coarse-grained lattice dielectric model for a solute embedded in a solid or liquid [28]. The interpretations developed for molecular solvation in that context carry over here.

[1] Lu, X. et al. Nanoimaging of Electronic Heterogeneity in Bi_2Se_3 and Sb_2Te_3 Nanocrystals. Advanced Electronic Materials **2018**, 4, 1700377.

[2] Atkin, J. M.; Berweger, S.; Jones, A. C.; Raschke, M. B. Nano-optical imaging and spectroscopy of order, phases, and domains in complex solids. Advances in Physics **2012**, 61, 745–842.

[3] Knoll, B.; Keilmann, F. Enhanced dielectric contrast in scattering-type scanning near-field optical microscopy. Optics Communications **2000**, 182, 321–328.

[4] Cvitkovic, A.; Ocelic, N.; Hillenbrand, R. Analytical model for quantitative prediction of material contrasts in scattering-type near-field optical microscopy. Optics Express **2007**, 15, 8550–8565.

[5] Govyadinov, A. A.; Amenabar, I.; Huth, F.; Carney, P. S.; Hillenbrand, R. Quantitative Measurement of Local Infrared Absorption and Dielectric Function with Tip-Enhanced Near-Field Microscopy. Journal of Physical Chemistry Letters **2013**, 4, 1526–1531.

[6] Ophus, C. Four-Dimensional Scanning Transmission Electron Microscopy (4D-STEM): From Scanning Nanodiffraction to Ptychography and Beyond. Microscopy and Microanalysis **2019**, 25, 563–582.

[7] Panova, O.; Ophus, C.; Takacs, C. J.; Bustillo, K. C.; Balhorn, L.; Salleo, A.; Balsara, N.; Minor, A. M. Diffraction imaging of nanocrystalline structures in organic semiconductor molec-

ular thin films. Nature Materials **2019**, 18, 860–865.

[8] Kresse, G.; Hafner, J. Ab initio molecular dynamics for liquid metals. Physical Review B **1993**, 47, 558–561.

[9] Kresse, G.; Hafner, J. Ab initio molecular-dynamics simulation of the liquid-metalamorphous-semiconductor transition in germanium. Physical Review B **1994**, 49, 14251–14269.

[10] Blöchl, P. E. Projector augmented-wave method. Physical Review B **1994**, 50, 17953–17979.

[11] Kresse, G.; Furthmüller, J. Efficiency of ab-initio total energy calculations for metals and semiconductors using a plane-wave basis set. Computational Materials Science **1996**, 6, 15–50.

[12] Kresse, G.; Furthmüller, J. Efficient iterative schemes for ab initio total-energy calculations using a plane-wave basis set. Physical Review B **1996**, 54, 11169–11186.

[13] Kresse, G.; Joubert, D. From ultrasoft pseudopotentials to the projector augmented-wave method. Physical Review B **1999**, 59, 1758–1775.

[14] Albinsson, B.; Michl, J. Anti, Ortho, and Gauche Conformers of Perfluoro-n-butane: Matrix-Isolation IR Spectra and Calculations. Journal of Physical Chemistry Letters **1996**, 100, 3418–3429.

[15] Gu, Y.; Wang, Z.; Peng, S.; Ma, T.; Luo, J. Quantitative measurement of transfer film thickness of PTFE based composites by infrared spectroscopy. Tribology International **2021**, 153, 106593.

[16] Hilborn, R. C. Einstein coefficients, cross sections, f values, dipole moments, and all that. arXiv **2002**, physics/0202029.

[17] Muller, E. A.; Gray, T. P.; Zhou, Z.; Cheng, X.; Khatib, O.; Bechtel, H. A.; Raschke, M. B. Vibrational exciton nanoimaging of phases and domains in porphyrin nanocrystals. Proceedings of the National Academy of Sciences **2020**, 117, 7030–7037.

[18] Wang, C.; Duscher, G.; Paddison, S. J. Electron energy loss spectroscopy of polytetrafluoroethylene: experiment and first principles calculations. Microscopy **2014**, 63, 73–83.

[19] Sweers, K.; van der Werf, K.; Bennink, M.; Subramaniam, V. Nanomechanical properties of α-synuclein amyloid fibrils: A comparative study by nanoindentation, harmonic force microscopy, and Peakforce QNM. Nanoscale Research Letters **2011**, 6, 270.

[20] Rosenberger, M. R.; Chen, S.; Prater, C. B. The use of the PeakForce$^{\mathrm{TM}}$ quantitative nanomechanical mapping AFM-based method for high-resolution Young's modulus measurement of

polymers. Measurement Science and Technology **2011**, 22, 125703.

[21] Pollard, B.; Raschke, M. B. Correlative infrared nanospectroscopic and nanomechanical imaging of block copolymer microdomains. Beilstein Journal of Nanotechnology **2016**, 7, 605–612.

[22] Aizpurua, J.; Taubner, T.; García de Abajo, F. J.; Brehm, M.; Hillenbrand, R. Substrate-enhanced infrared near-field spectroscopy. Optics Express **2008**, 16, 1529.

[23] Weeks, J. J.; Clark, E. S.; Eby, R. K. Crystal structure of the low temperature phase (II) of polytetrafluoroethylene. Polymer **1981**, 22, 1480–1486.

[24] Clark, E. S. The molecular conformations of polytetrafluoroethylene: forms II and IV. Polymer **1999**, 40, 4659–4665.

[25] Kubo, R. The fluctuation-dissipation theorem. Reports on Progress in Physics **1966**, 29, 255–284.

[26] Clark, E. S. The Crystal Structure of Polytetrafluoroethylene, Forms I and IV. Journal of Macromolecular Science B **2006**, 45, 201–213.

[27] Kobayashi, M.; Adachi, T. Polymorphism and Phase Transitions of Linear Oligomers of Polytetrafluoroethylene Revealed by Vibrational Spectroscopy. Journal of Physical Chemistry **1995**, 99, 4609–4619.

[28] Song, X.; Chandler, D.; Marcus, R. A. Gaussian field model of dielectric solvation dynamics. Journal of Physical Chemistry **1996**, 100, 11954–11959.